

# Imaging with Diffractive Axicons Rapidly Milled on Sapphire by Femtosecond Laser Ablation

**Daniel Smith**

Swinburne University of Technology - Hawthorn Campus: Swinburne University of Technology

**Soon Hock Ng**

Swinburne University of Technology - Hawthorn Campus: Swinburne University of Technology

**Molong Han**

Swinburne University of Technology - Hawthorn Campus: Swinburne University of Technology

**Tomas Katkus**

Swinburne University of Technology - Hawthorn Campus: Swinburne University of Technology

**Vijayakumar Anand** (✉ [physics.vijay@gmail.com](mailto:physics.vijay@gmail.com))

Swinburne University of Technology - Hawthorn Campus: Swinburne University of Technology

<https://orcid.org/0000-0001-8867-1949>

**Karl Glazebrook**

Swinburne University of Technology - Hawthorn Campus: Swinburne University of Technology

**Saulius Juodkazis**

Swinburne University of Technology - Hawthorn Campus: Swinburne University of Technology

---

## Research Article

**Keywords:** Femtosecond fabrication, Diffractive optical elements, Imaging, Computational optics, Incoherent optics.

**Posted Date:** October 12th, 2021

**DOI:** <https://doi.org/10.21203/rs.3.rs-680937/v1>

**License:**  This work is licensed under a Creative Commons Attribution 4.0 International License.

[Read Full License](#)

---

**Version of Record:** A version of this preprint was published at Applied Physics B on October 22nd, 2021. See the published version at <https://doi.org/10.1007/s00340-021-07701-x>.

1 **Imaging with Diffractive Axicons Rapidly**  
2 **Milled on Sapphire by Femtosecond Laser**  
3 **Ablation**

4 **DANIEL SMITH,<sup>1,4</sup> SOON HOCK NG,<sup>1,4</sup> MOLONG HAN,<sup>1,4</sup> TOMAS KATKUS,<sup>1</sup>**  
5 **VIJAYAKUMAR ANAND,<sup>1,\*</sup> KARL GLAZEBROOK,<sup>2</sup> AND SAULIUS JUODKAZIS<sup>1,3,</sup>**

6 <sup>1</sup>*Optical Sciences Centre and ARC Training Centre in Surface Engineering for Advanced Materials*  
7 *(SEAM), School of Science, Swinburne University of Technology, Hawthorn, VIC 3122, Australia.*

8 <sup>2</sup>*Centre for Astrophysics and Supercomputing, School of Science, Swinburne University of Technology,*  
9 *Hawthorn, VIC 3122, Australia.*

10 <sup>3</sup>*Tokyo Tech World Research Hub Initiative (WRHI), School of Materials and Chemical Technology,*  
11 *Tokyo Institute of Technology, 2-12-1, Ookayama, Meguro-ku, Tokyo 152-8550, Japan.*

12 <sup>4</sup>*The authors contributed equally to this work*

13 *\*vanand@swin.edu.au*

14 **Abstract:** Fabrication of large area (sub-1 cm cross-section) micro-optical components in a  
15 short period of time (~10 min) and with lesser number of processing steps is highly desirable  
16 and cost-effective. In the recent years, femtosecond laser fabrication technology has  
17 revolutionized the field of manufacturing by offering the above capabilities. In this study, a  
18 fundamental diffractive optical element, binary axicon – axicon with two phase or amplitude  
19 levels, has been designed in three configurations namely conventional axicon, photon sieve  
20 axicon (PSA) and sparse PSA and directly milled onto a Sapphire substrate. The fabrication  
21 results revealed that a single pulse burst fabrication can produce a flatter and smoother profile  
22 than pulse overlapped fabrication which gives rise to surface damage and increased roughness.  
23 The fabricated elements were processed in IsoPropyl Alcohol and Potassium Hydroxide to  
24 remove debris and redeposited amorphous Sapphire. An incoherent illumination was used for  
25 optical testing of the components and a non-linear optical filter was used for cleaning the noisy  
26 images generated by the diffractive optical elements.

27 **Keywords:** Femtosecond fabrication; Diffractive optical elements; Imaging; Computational optics;  
28 Incoherent optics.

29 **1. Introduction**

30 Generation and precise control of optical fields is crucial in many optical instruments and  
31 imaging systems [1]. The optical fields can be engineered using optical components belonging

32 to different categories such as refractive [2], diffractive [2], reflective [3], metaoptics [4-6],  
33 polarization optical components such as Q-plates [7], and liquid crystal optical components [8]  
34 based on the principle of operation. Depending upon the degree of control needed on the  
35 components of the optical field such as amplitude, phase and polarization, the complexity  
36 involved in design as well as fabrication varies. Next to the fully matured refractive optical  
37 technology, diffractive optics remains as the most widely used mode of beam control offering  
38 easier design, reasonable fabrication costs, and reaching diffraction efficiency closer to the  
39 values of refractive elements. Diffractive optics plays an important role in many areas of  
40 research such as optical trapping and tomography [9], computer generated holography [10],  
41 biomedical applications [11], integrated optics [12], display technology and serve also as  
42 components in augmented and mixed reality glasses [8].

43 The diffractive optical elements (DOEs) can be manufactured using different techniques  
44 such as photolithography [13], electron beam lithography [14], ion beam lithography [15],  
45 depending upon the feature sizes and area of the design. All of the above methods are not only  
46 time-consuming but also have higher operating costs resulting in an increase in the cost of the  
47 DOEs. Except ion beam lithography, the other two methods cannot fabricate elements directly  
48 on to the substrate and therefore, require additional processing steps such as reactive ion etching  
49 to transfer the pattern from the resist layer to the substrate which increases the cost of  
50 manufacturing further. The electron beam and ion beam lithography methods are not suitable  
51 for fabrication of large area DOEs. Even though it may be argued that photolithography can  
52 transfer large area patterns, the time is still spent on fabrication of the mask. Therefore, except  
53 for mass production, even photolithography cannot be considered as a rapid fabrication system.

54 In the recent years, there has been a revolution in manufacturing of DOEs due to the advent  
55 of femtosecond ablation techniques [16-19]. They not only offer capabilities to manufacture  
56 large area DOEs but also can reach subwavelength features by the generation of harmonics.  
57 Furthermore, the vacuum conditions and other environmental isolation needed for electron and

58 ion beam optics can be avoided in the femtosecond fabrication system. All of the above makes  
59 femtosecond fabrication systems superior to the existing methods on various technological and  
60 economical fronts. One current limitation of fs-laser fabrication is in its low capability to deliver  
61 practical solution for large area (mm-to-cm) scale micro-optical elements. This limitation is  
62 especially felt for large scale optical systems encountered in astronomy where meter-scale  
63 lenses and mirrors are used. For any optical system, the best light energy collection and transfer  
64 has to be achieved, which is handled via the best possible channeling of the etendue throughout  
65 the optical system from collection to detection (or imaging). The etendue  $E = S \times \Theta$  defined by  
66 the area  $S$  of the beam and the solid angle  $\Theta$  under which beam passes the surface. Optical  
67 elements with large surface area are required for best collection of light in low intensity light  
68 collection setups. Here we explore large area and fast laser fabrication which can become  
69 practical for astro-photonics.

70 In the recent years, there has been a shift in focus in imaging research from using coherent  
71 light sources to incoherent ones due to the many advantages such as broad applicability, low  
72 cost, and high resolving power [20]. A significant proportion of incoherent imagers are based  
73 on coded aperture imaging (CAI) method in which the light diffracted from an object was  
74 scattered and by computationally processing of the scattered intensity distributions with point  
75 spread functions (PSFs) the object information was reconstructed in multiple dimensions – 3D  
76 space and spectrum. The need for scattering makes CAI methods not suitable for power  
77 sensitive application areas such as fluorescence microscopy and astronomical imaging.  
78 Furthermore, the design and fabrication of a reasonably efficient coded aperture is complicated.  
79 In view of the above facts, in this study, a binary axicon is considered. Binary axicon has one  
80 of the simplest structures consisting of concentric rings with same period enabling easy design  
81 and fabrication. Binary axicon has a relatively higher signal to noise ratio than coded apertures  
82 and has a high focal depth capable of generating sharp object information from multiple planes  
83 on the sensor. An axicon has a low axial resolution and so it is difficult to discriminate

84 information from nearby planes as in CAI method. However, for cases like astronomical  
85 imaging, the object information is sparsely distributed and so an axicon may be suitable than a  
86 lens or a CAI method.

87 In this study, the femtosecond fabrication by ablation has been implemented to rapidly  
88 fabricate two-level axicons directly on to Sapphire substrates. The axicons were realized in  
89 conventional ring as well as sieve configurations. The focus of this study is on the rapid  
90 fabrication approach for manufacturing large area diffractive optical elements for astronomical  
91 imaging applications. This manuscript consists of four sections. The calculation of diffracted  
92 intensity distribution and the simulation results are presented in the next section. The third  
93 section contains the fabrication procedure and characterization and optical experiments and  
94 beam cleaning procedure. The summary and conclusion are presented in the final section.

## 95 **2. Methodology**

96 In most of the earlier studies on beam characteristics of axicon only a coherent illumination is  
97 considered [21-23]. In this study, the beam characteristics are investigated for a spatially  
98 incoherent illumination as it is easily available at a low cost and will be highly relevant to large  
99 scale and astronomical applications where large area devices are often required which in turn  
100 can be manufactured using femtosecond fabrication systems. For a single point object, the  
101 behaviour of a coherent light is like that of an incoherent one [20]. However, when there is  
102 more than one point, then the optical system differs hugely between coherent and incoherent  
103 illuminations. The optical configuration is shown in Fig. 1 in which the light diffracted from a  
104 point object is incident on a the diffractive axicon and the intensity distribution is recorded. The  
105 distance between the object and the axicon is  $u$  and the distance between the axicon and the  
106 sensor is  $v$ .

107

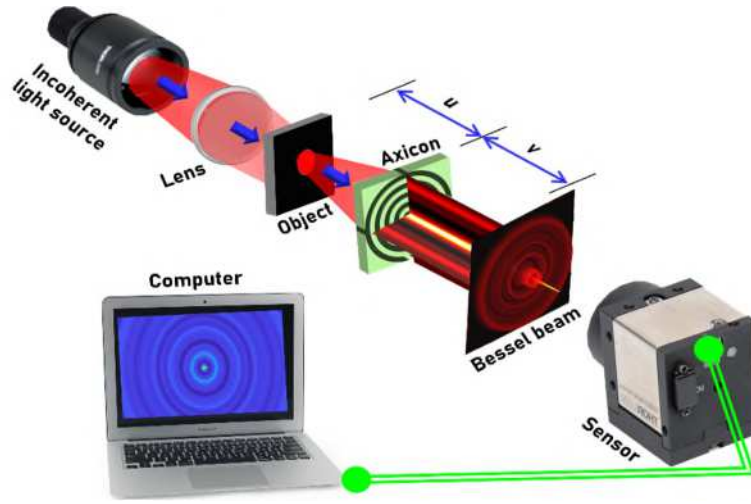


Fig. 1 Optical configuration for the generation of Bessel beams by a diffractive axicon

The binary axicon can be realized either as concentric rings or rings filled with discs similar to a photon sieve [24]. While the former with concentric rings has been widely used, only a few reports are available on axicons with sieve configuration. The rationale for comparing a conventional axicon with a photon sieve axicon (PSA) is that the fabrication using femtosecond ablation occurs point by point and it is much easier to realize an axicon as a PSA (disconnected discs) rather than in conventional type (overlapped discs). The radii of zones of a binary axicon can be given as

$$r_{1-n} = n\Lambda, \quad (1)$$

where  $\Lambda$  is the period of the axicon and  $n$  is an integer. The phase of a binary axicon can be expressed as

$$\Phi_{Axicon} = \begin{cases} \pi, & r_{1-n+1/2} \leq R \leq r_{1-n+1} \\ 0, & \text{elsewhere} \end{cases}, \text{ where } R = \sqrt{x^2 + y^2}. \quad (2)$$

The phase of a PSA is mathematically complicated as it is made up of circular discs of the same diameter instead of rings of varying diameters as in an axicon. A two-step process is proposed to design the PSA with polar coordinates  $(R, \varphi)$  where  $\varphi = \tan^{-1}(y/x)$ . In the first step, a mask consisting of Delta functions located at the  $x$  and  $y$  coordinates of the centers of

126 the discs of diameter  $\Lambda/2$  is generated. The centers of the circular discs can be located only at  
 127 specific radial values given as

$$128 \quad r_{2-n} = (4n - 1)\Lambda/4. \quad (3)$$

129 The circular discs cannot be tightly arranged in the ring of an axicon as the circumference  
 130 given as  $2\pi r_{2-n}$  cannot be an integral multiple of  $\Lambda$  for all values of  $r_{2-n}$ . The difference  
 131 between the above two values is given as

$$132 \quad L(r_{2-n}) = 2\pi r_{2-n} - \{floor(4\pi r_{2-n}/\Lambda)\}\Lambda/2, \quad (4)$$

133 where *floor* function converts an input real number  $x$  into the greatest integer less than or  
 134 equal to  $x$ . The increment in location needed for every disc is

$$135 \quad \Delta(r_{2-n}) = L(r_{2-n})/\{floor(4\pi r_{2-n}/\Lambda)\}. \quad (5)$$

136 The values of the angles are given as

$$137 \quad \theta_m(r_{2-n}) = [m\{\Lambda + \Delta(r_{2-n})\}]/r_{2-n}, \quad (6)$$

138 where  $m$  varies from 0 to  $floor(4\pi r_{2-n}/\Lambda)$ . The mask consisting of Delta functions is  
 139 given as

$$140 \quad Mask = \begin{cases} \delta, R = r_{2-n} \text{ and } \varphi = \theta_m \\ 0 \text{ elsewhere} \end{cases}. \quad (7)$$

141 At the end of the first step, the map of Delta functions is obtained for mounting the circular  
 142 discs in the next step. To generate the mask of PSA ( $M_{PSA}$ ), it is just sufficient to carry out a  
 143 2D convolution of the Mask function with a Circ function which is a circular top hat with a  
 144 radius given by

$$145 \quad M_{PSA} = Mask \otimes Circ(\Lambda/2), \quad (8)$$

146 where ' $\otimes$ ' is a 2D convolutional operator. The phase of the PSA is given as  $\Phi_{PSA} =$   
 147  $exp(j\pi M_{PSA})$ .

148 Let us consider a point object located at a distance of  $u$  from the diffractive axicon emitting  
 149 light with an amplitude of  $\sqrt{I_o}$ . The complex amplitude reaching the axicon is given as

$$150 \quad \psi_1 = C_1 \sqrt{I_o} Q(1/u) L(\bar{r}_o/u), \quad (9)$$

151 where

$$152 \quad Q(1/u) = \exp[j\pi R^2/(\lambda u)], \quad (10)$$

$$153 \quad L(\bar{o}/u) = \exp[j2\pi(o_x x + o_y y)/(\lambda u)], \quad (11)$$

154 and  $C_1$  is a complex constant and there is no linear phase associated with a point object in this  
155 case as the optical axis is assumed to match with the centres of all the optical elements. The  
156 complex amplitude after the binary axicon and PSA is given as

$$157 \quad \psi_2 = C_1 \sqrt{I_o} L(\bar{r}_o/u) Q(1/u) \exp(-j\Phi_{\text{DOE}}), \quad (12)$$

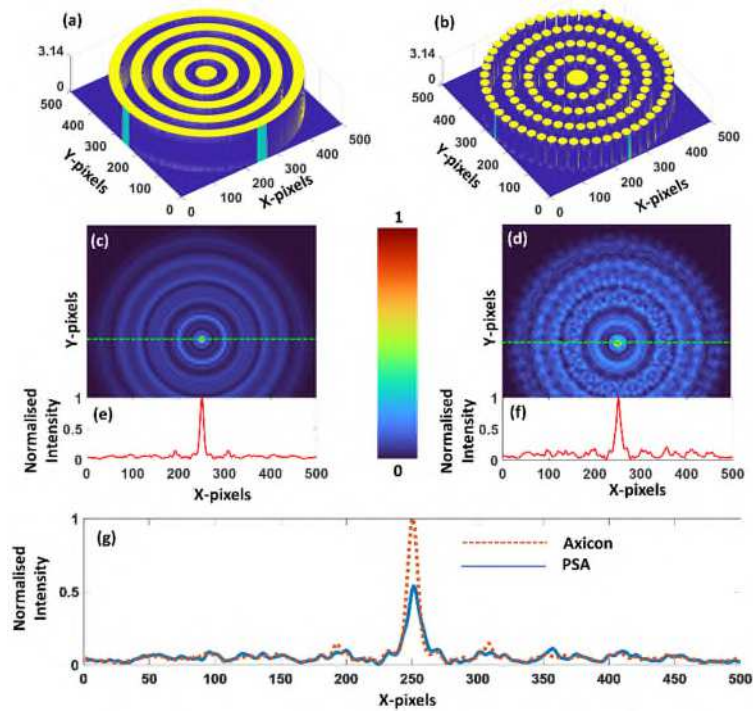
158 where  $\Phi_{\text{DOE}} = \Phi_{\text{Axicon}}$  when an axicon with concentric rings is used and  $\Phi_{\text{DOE}} = \Phi_{\text{PSA}}$  when  
159 an axicon with sieve configuration is used. The intensity pattern observed at a distance of  $v$   
160 from the DOE is given as a convolution of the complex amplitude with the quadratic phase  
161 function  $Q(1/v)$ ,

$$162 \quad I_v(\bar{r}_s; \bar{r}_o, u) = \left| C_1 \sqrt{I_o} L\left(\frac{\bar{r}_o}{u}\right) Q\left(\frac{1}{u}\right) \exp(-j\Phi_{\text{DOE}}) \otimes Q\left(\frac{1}{v}\right) \right|^2. \quad (13)$$

163 From Eq (13), if the  $\Phi_{\text{DOE}}$  equals  $(\pi R^2/\lambda)(1/u + 1/v)$ , then in the observation plane a  
164 focused point is obtained as the other phase components are cancelled. But for an axicon, the  
165 behaviour is quite interesting as it has constant radial spatial frequency. Within the focal depth  
166 of the axicon, there is always a radial region of the axicon which has a phase distribution same  
167 as  $(\pi R^2/\lambda)(1/u + 1/v)$ . This region is responsible for generating the central maximum of the  
168 Bessel function and the other radial regions which does not match the above phase distribution  
169 generate ring patterns around the central maximum. Higher the phase difference, the larger the  
170 diameter of the ring and the smaller is the energy density [25]. The intensity for a 2D object  $O$   
171 can be expressed as  $I_o = O \otimes I_v$ . Unlike a coherent source, where the complex amplitude is  
172 convolved, here only the intensity distribution is convolved as there is no spatial coherence  
173 present to generate the interference terms.  
174

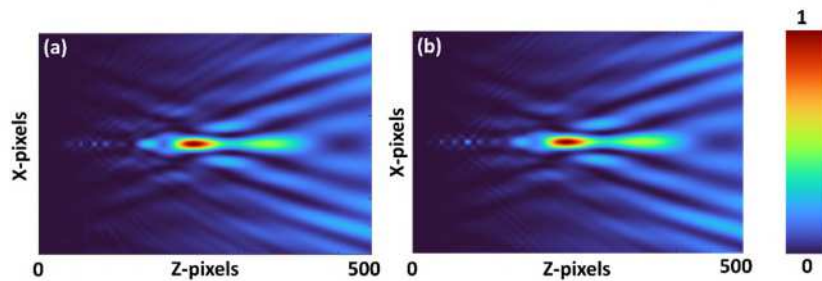
175       The images of the simulated axicon and PSA with same period are shown in Figs. 2(a) and  
176 2(b) respectively. The images of the diffraction pattern at the same distance for axicon and PSA  
177 are shown in Figs. 2(c) and 2(d) respectively and their normalised intensity profiles are shown  
178 in Figs. 2(e) and 2(f) respectively. There are interesting observations when comparing the  
179 diffraction patterns of axicon and PSA. The central maximum is sharper for axicon than PSA  
180 and the sidelobes of axicon appear less strong than that of the PSA. The two intensity  
181 distributions were normalised over the maximum of both and the intensity profile is compared  
182 as shown in Fig. 2(g). It is seen that axicon has a higher contrast of central maximum to the  
183 surrounding rings compared to that of PSA and the full width at half maximum (FWHM)  
184 obtained for axicon is smaller than that of PSA. This behaviour is different from the  
185 observations made with a Photon sieve Fresnel lens [26], where an improvement in the  
186 resolution was observed. The difference may be accounted to the difference between the areas  
187 of the two-phase levels. In the previous simulation studies, the areas were made equal to obtain  
188 the maximum efficiency in addition to maintaining the phase difference between two levels at  
189  $\pi$  for a two-level structure [2]. Due to the replacement of rings by circular discs, this condition  
190 cannot be met accurately. A previous study on PSA directly fabricated on the tip of optical fibre  
191 exhibited characteristics of an axicon [27]. To further evaluate the focal characteristics, the  
192 axial characteristics are studied for axicon and PSA under ideal conditions. The axial variation  
193 of the intensity distributions at ( $y=0$ ) line for axicon and PSA are shown in Figs. 3(a) and 3(b)  
194 respectively. Comparing the above two figures, it is seen that the performances are similar.  
195 From the simulation studies, it is seen that approximating a binary axicon using circular discs  
196 does not yield a better performance but reduces the contrast of the central maxima with respect  
197 to the surrounding ring patterns. However, the fabrication of PSA using femtosecond ablation  
198 is relatively easier than the fabrication of a conventional axicon.

199



200  
201  
202  
203  
204  
205

Fig. 2 Phase profile of (a) axicon and (b) PSA for a simulation wavelength  $\lambda = 617$  nm. Intensity distribution obtained for (c) axicon and (d) PSA. Locally normalised intensity profile of the line data ( $y=0$ ) for (e) axicon and (f) PSA. (g) Universally normalised intensity profile of the line data ( $y=0$ ) for axicon and PSA.



206  
207  
208  
209

Fig. 3 Locally normalised axial intensity distribution along the line ( $y=0$ ) for (a) axicon and (b) PSA.

210 The next step is to study the imaging performances of axicon and PSA using a test object.  
211 All experiments for this study have been carried out at Nanolab, Swinburne University and so  
212 the test object has been selected as the letters of “Nanolab” in arial font as shown in Fig. 4(a).  
213 The image of the object obtained using a Fresnel lens, axicon and PSA are shown in Figs. 4(b)-  
214 4(d) respectively. It is seen that the sidelobes generated by axicon affects the imaging quality  
215 drastically as expected and the results of PSA are distorted more than a conventional axicon.

216 Since the imaging system using PSA is a linear shift-invariant system, it is possible to obtain  
217 an image without the background noise using cross-correlation with the point spread function  
218 (PSF). Cross-correlation is one of the most widely used reconstruction methods used in coded  
219 aperture imaging systems such as coded aperture correlation holography (COACH) [28] and  
220 interferenceless-COACH (I-COACH) [29]. Recently, it was found that non-linear  
221 reconstruction method was the optimal correlation-based reconstruction method for scattering  
222 based linear shift-invariant system [30]. Can the NLR be applied to this method of imaging  
223 using PSA?

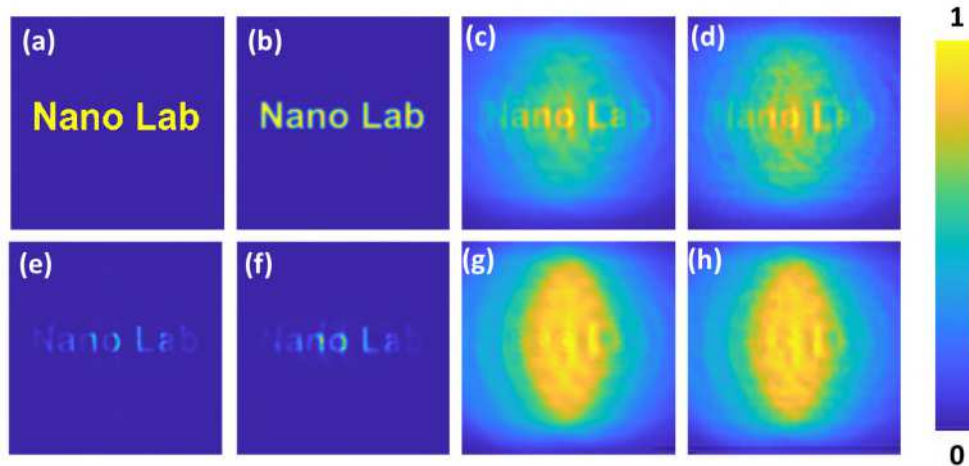
224 In I-COACH, every point in the object space is mapped to a random intensity distribution  
225 in the sensor plane. When there are many points in the same plane, every point generates the  
226 same random intensity distribution but shifted depending upon the linear phase they possess.  
227 In an incoherent imaging system, these random intensity distributions are summed. This is the  
228 meaning of linear shift invariant system in intensity. In I-COACH, when the point object is  
229 axially shifted, the random intensity distribution changes. In the current system, every point in  
230 the object space is mapped to a Bessel-like intensity distribution. When there are many points,  
231 shifted Bessel-like intensity distributions are generated depending upon the linear phase and all  
232 such Bessel-like intensity distributions are summed in the sensor plane. However, unlike I-  
233 COACH, when the axial location is changed, the intensity distribution does not vary within the  
234 focal depth. In both I-COACH and the imaging with PSA, the object information can be  
235 reconstructed by a cross-correlation between the multi-points intensity distribution and the PSF.  
236 In I-COACH, to reconstruct the object at a different plane, the PSF at that plane is needed. In  
237 imaging with PSA, different planes of the object can be reconstructed using the same PSF. Non-  
238 linear reconstruction is the optimal correlation obtained by tuning the magnitudes of spectrum  
239 of the object intensity and PSF until a minimum entropy is obtained. This approach can be  
240 applied to any linear shift-invariant system. NLR is a pattern recognition operation with a  
241 physical meaning of scanning the PSF over the object intensity pattern and finding the value of

242 similarity at every location. So, while applying NLR, a Bessel-like intensity pattern obtained  
 243 for a single point (by PSA) is once again converted into a point. Consequently, an image with  
 244 background is converted to an image without background during this operation yielding a  
 245 cleaner image. This is the rationale for applying NLR to this method [30-32].

246

247 The cleaned image by NLR is given as  $I_R =$   
 248  $\left| \mathcal{F}^{-1} \left\{ |\tilde{I}_v|^\alpha \exp[i \arg(\tilde{I}_v)] |\tilde{I}_o|^\beta \exp[-i \arg(\tilde{I}_o)] \right\} \right|$ , where  $\alpha$  and  $\beta$  are tuned to obtain the  
 249 lowest entropy and  $\arg$  refers to the phase. The images generated by axicon and PSA after  
 250 applying NLR is shown in Figs. 4(e) and 4(f) respectively. To show the difference between the  
 251 use of coherent and incoherent illumination, the results obtained for coherent light source for  
 252 an axicon and PSA are shown in Figs. 4(g) and 4(h) respectively. Comparing the results  
 253 obtained for spatially incoherent light with those of coherent light, the quality of images was  
 254 found to be better for spatially incoherent illumination than coherent due to the lack of mutual  
 255 interference.

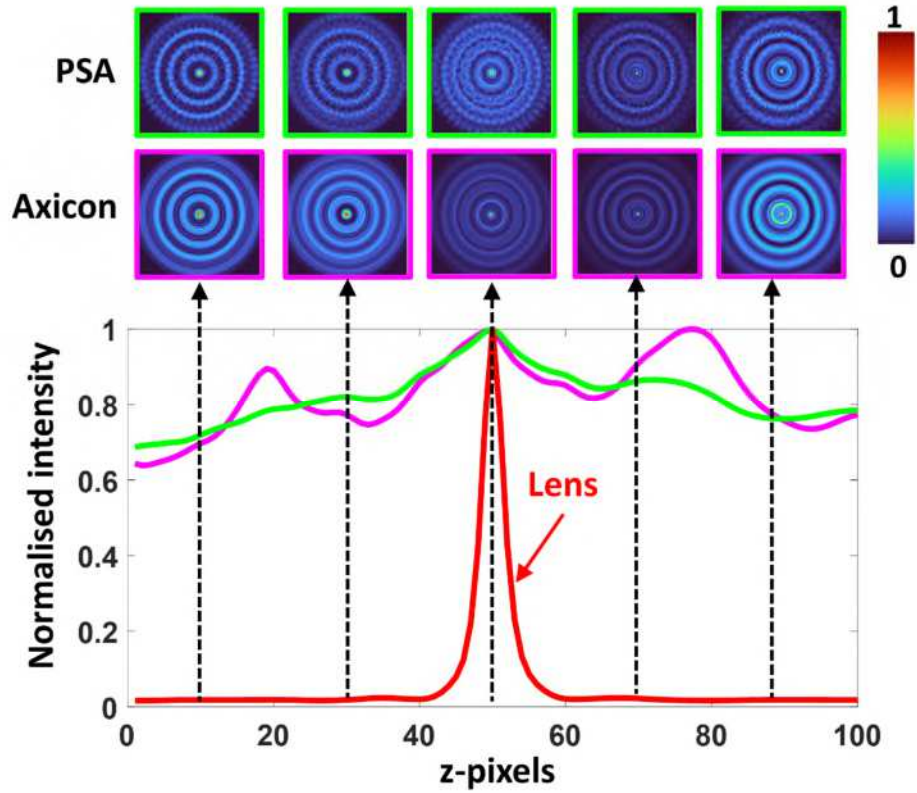
256



257  
 258  
 259  
 260  
 261  
 262

Fig. 4 Image of the (a) test object. Image of the object generated by a (b) Fresnel lens, (c) axicon and (d) PSA. Computationally cleaned image by applying NLR for (e) axicon and (f) PSA. The images obtained for coherent illumination for (g) axicon and (h) NLR.

263 Another important observation is that the intensity distribution of axicon and PSA are similar  
264 in the central region while they are quite different at the outer regions (refer Fig. 2). The random  
265 change in the location of the discs and the spacing between the discs at every consecutive zone  
266 disturbs the diffraction pattern resulting in the interesting intensity distribution for PSA. To  
267 understand the axial characteristics of axicon and PSA, the intensity distribution  $I_\nu$  was  
268 simulated for different distances of  $\nu$  from  $\nu-\Delta$  to  $\nu+\Delta$  and cross-correlated with the intensity  
269 distribution at  $\nu$  as  $I_\nu * I_{\nu+\Delta}$ , where ‘\*’ is a 2D correlation operator. The intensity distributions  
270 for some distances and the plot of the axial correlation values are shown for both axicon and  
271 PSA in Fig. 5. The case for a diffractive lens is shown for reference. From this study, it seems  
272 that a PSA has a higher axial resolution than an axicon. The randomness associated with the  
273 distribution of disc suppresses the peaks around the central maximum. From an imaging point  
274 of view, the PSA has a slightly better performance than an axicon. When imaging a thick object  
275 and focusing a plane of that object, the information from other planes will be of slightly lower  
276 intensity in the case of PSA when compared to an axicon. Compared to a lens, both PSA and  
277 axicon have a significantly lower axial resolution. However, the intended area of application  
278 i.e., 3D imaging of sparse objects, the high focal depth of PSA and axicon will be useful.  
279



280

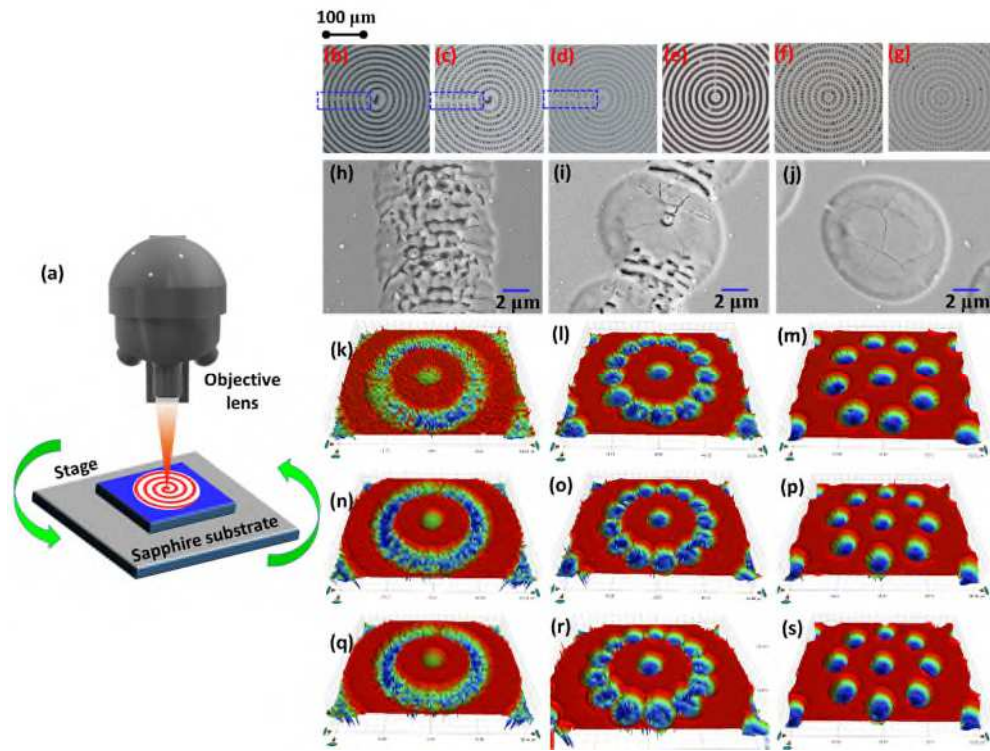
281 Fig. 5 Plot of  $I_V^* I_{V\pm\Delta}$  for different distances for axicon (pink), PSA (green) and a lens (red). The intensity  
 282 distributions for axicon, and PSA for some distances have been provided.

### 283 3. Experiments

#### 284 3.1 Fabrication

285 The fabrication was carried out on sapphire substrate with a thickness of 500  $\mu\text{m}$  and index of  
 286 refraction  $n_s = 1.76$ . In order to have  $\pi$  phase difference between the two levels the thickness  
 287 needed to be milled is given as  $t = \lambda/2(n_s-1)$  which is  $\sim 0.41 \mu\text{m}$  for  $\lambda = 617 \text{ nm}$  which is the  
 288 wavelength of the source used for optical testing. The substrate was cleaned prior to fabrication  
 289 with acetone and iso-propyl alcohol (IPA) and blown dry. Three optical devices, namely an  
 290 axicon, a PSA and a sparse PSA were fabricated. The fabrication was carried out using a Pharos  
 291 laser (Light Conversion, Lithuania) operating at 200 kHz repetition rate,  $\lambda = 1030 \text{ nm}$   
 292 wavelength, 2.5W average power, 230 fs pulse duration and 5 $\times$  magnification, NA = 0.14  
 293 numerical aperture Mitutoyo Plan Apo NIR infinity corrected objective. Two pulse bursts per  
 294 ablation spot was used (with an exception for the axicon that did not use a pulse burst) in

295 combination with pulse energy after the objective attenuated to 5  $\mu\text{J}$  to achieve the design  
296 ablation depth and the ablated spot diameter of  $d = 8.9 \mu\text{m}$ . The diameter of ablated spot was  
297 closely matching the diameter for the used NA:  $d = 2w = 1.22\lambda/\text{NA}$ , where  $w$  is the waist of the  
298 beam at focus. The peak intensity of a 5  $\mu\text{J}$  pulse (peak intensity is twice the average) is 69  
299  $\text{TW}/\text{cm}^2$  at the fluence of  $16 \text{ J}/\text{cm}^2$ . This is markedly larger than the ablation threshold of  
300 sapphire at  $\sim 2 \text{ J}/\text{cm}^2$  and  $\sim 10 \text{ TW}/\text{cm}^2$ . The speed of Aerotech positioning stages was set to 2  
301  $\text{mm}/\text{s}$ . Stage travel with position sensitive output (PSO) mode was used to ensure accurate pulse  
302 spacing. The fabrication code was written in SCA software (Workshop of Photonics Altechna,  
303 Lithuania). The code comprised of concentric circle commands with circle radius increasing by  
304  $16 \mu\text{m}$  till the overall design diameter reached 5 mm. Laser pulse spacing in a given circle was  
305 set to be 5  $\mu\text{m}$ , 8  $\mu\text{m}$ , and 12  $\mu\text{m}$  for respectively the axicon, the PSA, and the sparse PSA  
306 fabrications. The Pharos system unlike electron beam lithography system always works in fixed  
307 beam movable stage mode (FBMS) mode which is a special case in lithography systems such  
308 as RAITH150<sup>2</sup>. Conventional raster and serpentine scanning approaches are time consuming as  
309 every pixel of the design must be scanned. In this study, time efficient circular scanning  
310 procedure was selected where the pixel locations were selected for the beam to traverse and the  
311 stage was moved only to those locations as shown in Fig. 6(a). The scanning procedure started  
312 from the centre and moved gradually outward following the coordinate map. In this way, the  
313 fabrication time was reduced by at least half of that of conventional scanning approaches. The  
314 fabrication time for the sparse PSA, PSA and axicon was approximately 10 minutes. When the  
315 stage moved to the coordinates, a laser pulse (single pass) ablates the corresponding voxels  
316 (volume element, i.e., a 3D pixel).



317  
 318 Fig. 6 (a) Schematic of the scanning procedure. Optical microscope images of the central part  
 319 of (b) axicon, (c) PSA and (d) sparse PSA with stitching and stigmatism errors. Optical  
 320 microscope images of the central part of (e) axicon, (f) PSA and (g) sparse PSA after the  
 321 correction of stitching and stigmatism errors. SEM images of a single pulse fabrication for (h)  
 322 axicon, (i) PSA and (j) sparse PSA; ripples with period  $\sim 1 \mu\text{m} \approx \lambda$  are recognizable in the  
 323 strongly overlapped pulse exposure regions. Surface profiles of (k) axicon, (l) PSA and (m)  
 324 sparse PSA, after femtosecond fabrication. Surface profiles of (n) axicon, (o) PSA and (p)  
 325 sparse PSA after ultrasonic cleaning in IPA and surface profiles of (q) axicon, (r) PSA and (s)  
 326 sparse PSA after KOH etching.

327

328 In the first step, the effect of stitching error arising due to the condition that the

329 circumference of the zones is not equal to the integral multiples of  $\Lambda/2$ . The optical microscope

330 images of the fabricated axicon, PSA and sparse PSA are shown in Figs. 6(b)-6(d) respectively.

331 The stitching error is clearly visible. In addition to the stitching error there was error due to

332 stigmatism in the stage resulting in oval shaped zones. The error compensation terms were

333 introduced in the code to reduce both the stitching error and stigmatism. The optical microscope

334 images after correction are shown in Figs. 6(e)-6(g) respectively. The SEM images of a single

335 disc for axicon, PSA and sparse PSA are shown in Figs. 6(h)-6(j). It can be seen that with the

336 overlap of pulses in PSA and axicon, the surface is damaged more and becomes rough due to

337 ripple formation [33] while the sparse PSA without disc overlap has a smoother and nearly flat  
338 surface with only cracks visible at the molten region on the bottom. A fast thermal quenching  
339 of shallow melt pool is the most probable cause of formation of nano-cracks; note the melting  
340 temperature of sapphire is 2040°C. A remarkable feature of the used two-pulse ablation was a  
341 flat bottom of the ablation pit. The apparent melting was contributing to the flatness of ablation  
342 site; however, the other contribution should be in the profile of energy deposition. The die-met  
343 transition, when dielectric is transferred to the metallic plasma state with permittivity  
344 decreasing to  $\varepsilon = n^2 = 0$  at the dielectric breakdown [34], is defining the lateral absorption  
345 profile. For a Gaussian-like intensity at the focus, the most intense central region is turning into  
346 the most reflective during the laser pulse, hence, less energy is deposited to the sample. This  
347 qualitatively explains the ablation profile which would be expected for a hat-top intensity  
348 profile (rather than the Gaussian). The detailed mechanism of ablation is out of scope of this  
349 study focused on optical performance, however, is worth of a deeper investigation.

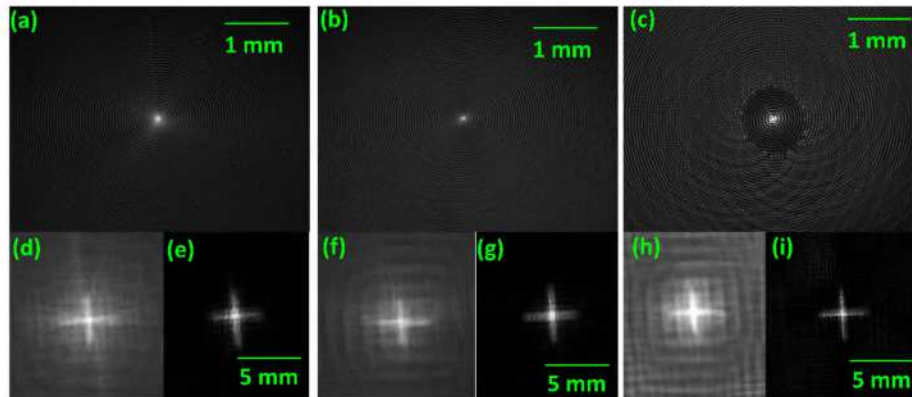
350 The rough surfaces of PSA and axicon are expected to scatter light more resulting in lower  
351 efficiency in the first diffraction order. After fabrication, it was noted that there was  
352 redeposition of debris both on the milled and unmilled areas of the device. Two step cleaning  
353 procedures were carried out. After femtosecond fabrication, the sample was cleaned in IPA in  
354 the ultrasonic bath for 5 minutes. The surface profiles of the axicon, PSA and sparse PSA before  
355 and after cleaning are shown in Figs. 6(k)-6(p) respectively. After the first cleaning, most of  
356 the debris are removed. The next cleaning was carried out with a KOH solution with (2M  
357 concentration for 2 hrs) to remove the redeposited amorphous Sapphire and there was further  
358 improvement rendering an even smoother profile [35] for axicon, PSA and sparse PSA as  
359 shown in Figs. 6(q)-6(s). The average depth values measured for the axicon, PSA and sparse  
360 PSA were 360 nm, 416 nm, 420 nm respectively. This required depth for a  $\pi$ -phase shift was  
361 achieved in a two-pulse irradiation without change of the focal position. The Rayleigh length  
362 (half of depth-of-focus DOF) is  $z_R = \pi w^2 / \lambda = 61.4 \mu\text{m}$ . This large DOF increase tolerance of

363 high-fidelity fabrication over large areas when some tilt of a surface plane can be expected. The  
364 dark regions in the microscope images and the higher roughness in surface profiles indicates  
365 that there was some amount of redeposition of the material into the ablated area due to the  
366 overlap of the voxels during fabrication. This redeposition is dependent upon various factors  
367 such as the pulse energy, material characteristics such as melting point, crystalline or  
368 amorphous.

### 369 *3.2 Optical testing*

370 The optical testing was carried out using a high-power LED from Thorlabs (M617L3,  $\lambda_c = 617$   
371 nm, full width at half maximum (FWHM) = 18 nm) and a spectral filter was used at 600 nm  
372 with a width of 10 nm to improve the temporal coherence. A pinhole with a size of 100  $\mu\text{m}$  and  
373 a cross-shaped object were used for imaging. A 3 $\times$  magnifying system was used to reimage the  
374 intensity distribution that is close to the DOEs on an image sensor (Thorlabs DCU223M, 1024  
375 pixels  $\times$  768 pixels, pixel size = 4.65  $\mu\text{m}$ ). The DOEs were mounted one after the other and the  
376 intensity distributions were recorded. The intensity distributions recorded at a distance of 5 mm  
377 for the axicon, PSA and sparse PSA are shown in Figs. 7(a)-7(c) respectively. A cross object  
378 was then mounted instead of the pinhole and the intensity patterns were recorded at 3 cm from  
379 the DOEs. The images of the cross object recorded for the axicon, PSA and sparse PSA are  
380 shown in Figs. 7(d), 7(f) and 7(h) respectively. The images were cleaned using the images  
381 obtained for a pinhole and the NLR method and the cleaned images are shown in Figs. 7(e),  
382 7(g) and 7(i) respectively. To improve the cleaning results, additional filters such as median  
383 filter and correlation filters were used as demonstrated in [36]. The images after cleaning for  
384 axicon, PSA and sparse PSA appear similar.

385  
386

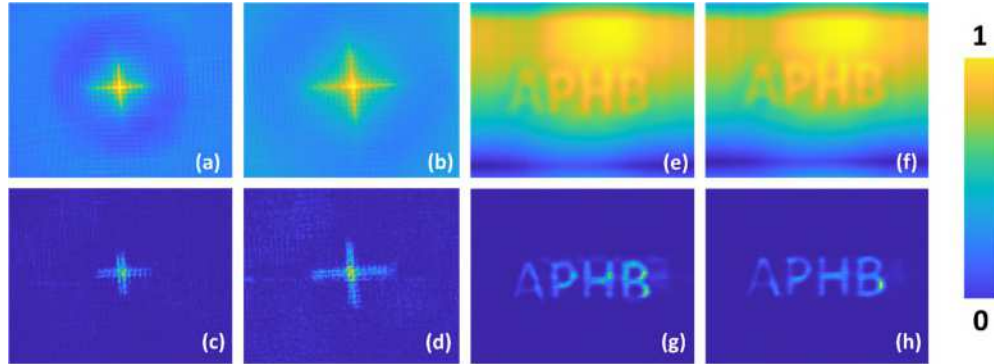


387  
 388 Fig. 7 Intensity distributions recorded for a pinhole at distances 5 mm for (a) axicon, (b) PSA and (c)  
 389 sparse PSA. Recorded intensity distributions for a cross shaped transmission object at 5 mm for (d) axicon,  
 390 (f) PSA and (h) sparse PSA. Cleaned images of cross for (e) axicon, (g) PSA and (i) sparse PSA.

391

392 Therefore, it is feasible to use a sparse axicon instead of a regular axicon for imaging  
 393 applications. By virtue of a wide spectral transparency of sapphire from UV to IR, optical  
 394 elements with ~1 cm cross section can be made within ~10 min which allows for a wider use  
 395 of such prototyping for more complex optical systems. It must be noted that the cleaning  
 396 procedure does not require the recording of the PSF exactly at the same location as the object  
 397 owing to the high focal depth of the imager. For the same reason, while cleaning images of  
 398 thick objects the planes that are out of focus will have a higher intensity as the plane in focus.  
 399 Consequently, if the information of two planes overlap laterally then the information could not  
 400 be perceived accurately. The PSF recorded at a single plane can be used to clean the image  
 401 information corresponding to many planes due to the high focal depth of PSA and axicon. The  
 402 image cleaning results for the intensity distributions recorded for the cross object at 5 cm (Fig.  
 403 8(a)) and 6 cm (Fig. 8(b)) using pinhole intensity distributions recorded at 5 mm are shown for  
 404 axicon and PSA as shown in Fig. 8(c) and 8(d) respectively. Since the cross object is a simple  
 405 object, the cleaning may not appear significant. A synthetic object consisting of the letters  
 406 'APHB' was used next and the corresponding intensity distributions for PSA were synthesized  
 407 by convolving the intensity distributions recorded for a pinhole with the object function. The  
 408 intensity distribution of the synthetic object at two planes 5 cm and 6 cm are shown in Fig. 8(e)

409 and 8(f) respectively. The cleaned images using the pinhole recording at 5 mm are shown in  
410 Figs. 8(g) and 8(h) respectively.



411  
412 Figure. 8 Intensity distribution of cross object recorded at (a)  $z = 5$  cm and (c)  $z = 6$  cm and the  
413 corresponding cleaned images (c)  $z = 5$  cm and (d)  $z = 6$  cm respectively. Intensity distribution  
414 of synthetic object 'APHB' recorded at (e)  $z = 5$  cm and (f)  $z = 6$  cm and the corresponding  
415 cleaned images (g)  $z = 5$  cm and (h)  $z = 6$  cm respectively.  
416

#### 417 4. Conclusion

418 Rapid fabrication of large area DOEs using the femtosecond laser fabrication system has been  
419 investigated. A simpler design with the function of a binary axicon was used for the study. The  
420 fabrication time was only 10 minutes using the femtosecond fabrication method for a large area  
421 of  $5 \text{ mm} \times 5 \text{ mm}$ . The binary axicon was realized in three configurations namely conventional  
422 axicon, PSA and sparse PSA. It was noticed that when the beam overlaps during milling results  
423 in redeposition of material resulting in a lower depth than the case without beam overlap which  
424 goes against the common belief that overall higher exposure with beam overlap increases the  
425 depth. In addition, the case with beam overlap has a higher roughness value than the case  
426 without beam overlap. This increase in roughness is partly contributed by the redeposition and  
427 partly due to light-matter interaction at temperature changes caused by ablation by the previous  
428 pulse. Reduction of debris and mechanism of ripple-free deep ablation at high irradiance which  
429 exceeds ablation threshold more than an order of magnitude are directions for future  
430 investigations which were not practical at low repetition rates [37].

431 One interesting outcome of this study is that it seems it may be necessary to approximate  
432 the design of the DOE functions as in this case where a sieve configuration was used instead of

433 rings to achieve a milling favorable design. As is seen in this study, the intensity distributions  
434 obtained for the sieve configuration is similar to that of the conventional axicon with a slight  
435 loss of lateral resolution and increase in axial resolution. Therefore, it should be possible to  
436 modify the design of DOEs without compromising the diffraction performances and at the same  
437 time achieve high fabrication accuracy without material redeposition and increase in surface  
438 roughness.

439 Some of the recent studies on controlling the distribution of debris using externally applied  
440 electric and magnetic fields offer opportunities to control the light-matter interactions and  
441 achieve better fabrication results [38,39]. We believe that the direction of research will enable  
442 the fabrication of large area structures suitable for incoherent illumination and astronomical  
443 imaging applications. With the introduction of spatial multiplexing [40], optimization [41] and  
444 redesigning of DOEs, the performance of the femtosecond fabrication system can be improved  
445 further. Astronomical imaging is one of the areas which require large area optical devices with  
446 capabilities to perform a high signal to noise ratio. We believe that the femtosecond ablation  
447 based rapid fabrication and computational optics in tandem will lead to the development of  
448 advanced astronomical imaging technologies. Some of the latest developments in astronomical  
449 spectral imaging technologies such as FOBOS [42] require numerous micro-optical devices for  
450 the successful implementation of free space to fiber bundle coupling for spectral imaging. We  
451 believe that the current work consisting of rapid fabrication and beam cleaning will support  
452 retrieving spatial information in addition to the recorded spectral information [43].

453 **Funding.** ARC LP190100505 is acknowledged for funding.

454 **Acknowledgments.** We are grateful to the Workshop of Photonics, Ltd. for femtosecond laser fabrication system  
455 acquired via technology transfer project. We acknowledge funding for the Nanolab by Swinburne University of  
456 Technology (SUT). DS is grateful for support via Honors and MH via PhD programs at SUT.

457 **Disclosures.** The authors declare no conflicts of interest.

458 **Data availability.** The datasets used and/or analysed during the current study are available from the corresponding  
459 author on reasonable request.

460  
461 **List of abbreviations:** PSA – Photon sieve axicon; DOE – Diffractive optical elements; FWHM – Full width at half  
462 maximum; NLR – Non-linear reconstruction; IPA – Isopropyl alcohol; LED – Light emitting diode; DOF – Depth of  
463 focus; M – Molar; KOH – Potassium hydroxide; SEM – Scanning electron microscope; UV – Ultraviolet; IR – Infrared;

464 FBMS – Fixed beam movable stage; M – Molar; NIR – Near infrared; NA – Numerical aperture; PSO – Position  
465 sensitive output.

466  
467 **Author contributions:** Light matter interaction and dynamics conceptualization – S. J; Fabrication – D.S, S.H.N, M.  
468 H and T. K; Characterisation – M. H, D. S, S.H.N, V. A and T. K. KOH etching – S. H. N, V. A and D. S; Simulation  
469 – V. A and D. S; Optical testing – V. A, S. H. N and D. S; Manuscript writing – V. A and S. J; Review, editing and  
470 proof reading – all the authors; Project guidance – K. G, S. J; Resources – S. J; Funding – S. J.

## 471 References

- 472 1. Dickey, FM, Holswade, SC, and Shealy, DL, eds., (2005), *Laser Beam Shaping Applications*, CRC Press.
- 473 2. Vijayakumar, A and Bhattacharya, S, (2017) *Design and Fabrication of Diffractive Optical Elements with*  
474 *MATLAB*.
- 475 3. Liang, J., Kohn, Jr., R. N., Becker, M. F., & Heinzen, D. J. (2010). High-precision laser beam shaping using a  
476 binary-amplitude spatial light modulator. *Appl. Opt.*, 49(8), 1323–1330. <https://doi.org/10.1364/ao.49.001323>.
- 477 4. Wang, L., Kruk, S., Tang, H., Li, T., Kravchenko, I., Neshev, D. N., & Kivshar, Y. S. (2016). Grayscale  
478 transparent metasurface holograms. *Optica*, 3(12), 1504–1505. <https://doi.org/10.1364/optica.3.001504>.
- 479 5. Epstein, A., & Eleftheriades, G. V. (2016). Huygens' metasurfaces via the equivalence principle: design  
480 and applications. *J. Opt. Soc. of Am. B*, 33(2), A31–A50. <https://doi.org/10.1364/josab.33.000a31>.
- 481 6. Kildishev, A. V., Boltasseva, A., & Shalaev, V. M. (2013). Planar Photonics with Metasurfaces. *Science*,  
482 339(6125), 1232009–1232009. <https://doi.org/10.1126/science.1232009>.
- 483 7. Rubano, A., Cardano, F., Piccirillo, B., & Marrucci, L. (2019). Q-plate technology: a progress review [Invited].  
484 *J. Opt. Soc. of Am. B*, 36(5), D70–D87. <https://doi.org/10.1364/josab.36.000d70>.
- 485 8. Li, Y., Zhan, T., Yang, Z., Xu, C., LiKamWa, P. L., Li, K., & Wu, S.-T. (2021). Broadband cholesteric liquid  
486 crystal lens for chromatic aberration correction in catadioptric virtual reality optics. *Opt. Express*, 29(4), 6011–  
487 6020. <https://doi.org/10.1364/oe.419595>.
- 488 9. Vijayakumar, A., Vinoth, B., Minin, I. V., Rosen, J., Minin, O. V., & Cheng, C.-J. (2017). Experimental  
489 demonstration of square Fresnel zone plate with chiral side lobes. *Appl. Opt.*, 56(13), F128–F133.  
490 <https://doi.org/10.1364/ao.56.00f128>.
- 491 10. Bruder, F.-K., Fäcke, T., Hagen, R., Hönel, D., Kleinschmidt, T. P., Orselli, E., Rewitz, C., Rölle, T., & Walze,  
492 G. (2015). Diffractive optics in large sizes: computer-generated holograms (CGH) based on Bayfol HX  
493 photopolymer. *Advances in Display Technologies V*. <https://doi.org/10.1117/12.2077139>.
- 494 11. Jahns and S. Sinzinger. (2000). Microoptics for biomedical applications. *Am. Biotechnol. Lab.* **11**, 53-54.
- 495 12. Jahns, J., & Huang, A. (1989). Planar integration of free-space optical components. *Appl. Opt.*, 28(9), 1602–  
496 1605. <https://doi.org/10.1364/ao.28.001602>.
- 497 13. Misawa, H., Kondo, T., Juodkazis, S., Mizeikis, V., & Matsuo, S. (2006). Holographic lithography of periodic  
498 two- and three-dimensional microstructures in photoresist SU-8. *Opt. Express*, 14(17), 7943–7953.  
499 <https://doi.org/10.1364/oe.14.007943>.
- 500 14. Anand, V., Ng, S. H., Katkus, T., Juodkazis, S. (2021). White light three-dimensional imaging using a quasi-  
501 random lens. *Opt. Express*, 29(10), 15551–15563. <https://doi.org/10.1364/oe.426021>.
- 502 15. Seniutinas, G., Gervinskas, G., Anguita, J., Hakobyan, D., Brasselet, E., Juodkazis, S. (2016). Nano-proximity  
503 direct ion beam writing. *Nanofabrication*, 2(1), 54–62. <https://doi.org/10.1515/nanofab-2015-0006>.
- 504 16. Marcinkevičius, A., Juodkazis, S., Watanabe, M., Miwa, M., Matsuo, S., Misawa, H., Nishii, J. (2001).  
505 Femtosecond laser-assisted three-dimensional microfabrication in silica. *Opt. Lett.*, 26(5), 277–279.  
506 <https://doi.org/10.1364/ol.26.000277>.
- 507 17. Malinauskas, M., Žukauskas, A., Hasegawa, S., Hayasaki, Y., Mizeikis, V., Buividas, R., Juodkazis, S. (2016).  
508 Ultrafast laser processing of materials: from science to industry. *Light: Sci. Appl.*, 5(8), e16133.  
509 <https://doi.org/10.1038/lsa.2016.133>.
- 510 18. Juodkazis, S., Yamasaki, K., Mizeikis, V., Matsuo, S., Misawa, H. (2004). Formation of embedded patterns in  
511 glasses using femtosecond irradiation. *Appl. Phys. A*, 79, 1549–1553. <https://doi.org/10.1007/s00339-004-2845-1>.
- 512 19. Vanagas, E., Kudryashov, I., Tuzhilin, D., Juodkazis, S., Matsuo, S., Misawa, H. (2003). Surface  
513 nanostructuring of borosilicate glass by femtosecond nJ energy pulses. *Appl. Phys. Lett.*, 82(17), 2901–2903.  
514 <https://doi.org/10.1063/1.1570514>.
- 515 20. Rosen, J., Vijayakumar, A., Kumar, M., Rai, M. R., Kelner, R., Kashter, Y., Bulbul, A., Mukherjee, S. (2019).  
516 Recent advances in self-interference incoherent digital holography. *Adv. Opt. Photon.*, 11(1), 1–66.  
517 <https://doi.org/10.1364/aop.11.000001>.
- 518 21. Kizuka, Y., Yamaguchi, M., Matsuoka, Y. (2008). Characteristics of a laser beam spot focused by a binary  
519 diffractive axicon. *Opt. Eng.*, 47(5), 053401. <https://doi.org/10.1117/1.2919739>.
- 520 22. Khonina, S. N., Porfirev, A. P. (2018). 3D transformations of light fields in the focal region implemented by  
521 diffractive axicons. *Appl. Phys. B*, 124(9), 1–13. <https://doi.org/10.1007/s00340-018-7060-4>.
- 522 23. Gervinskas, G., Seniutinas, G., Vijayakumar, A., Bhattacharya, S., Jelmakas, E., Kadys, A., Tomašiūnas, R.,  
523 Juodkazis, S. (2013). Fabrication and replication of micro-optical structures for growth of GaN-based light  
524 emitting diodes. *Micro/Nano Materials, Devices, and Systems*. <https://doi.org/10.1117/12.2033709>.
- 525 24. Andersen, G., Tullson, D. (2007). Broadband antihole photon sieve telescope. *Appl. Opt.*, 46(18), 3706–3708.  
526 <https://doi.org/10.1364/ao.46.003706>.
- 527

- 528  
529  
530  
531  
532  
533  
534  
535  
536  
537  
538  
539  
540  
541  
542  
543  
544  
545  
546  
547  
548  
549  
550  
551  
552  
553  
554  
555  
556  
557  
558  
559  
560  
561  
562  
563  
564  
565  
566  
567  
568  
569  
570  
571  
572  
573  
574  
575  
576  
577  
578
25. Anand, V., et. al. (2021). All Femtosecond Optical Pump and X-Ray Probe: Holey-Axicon for Free Electron Laser, *J. Phys. Photonics*, 3(2), 024002. <https://doi.org/10.1088/2515-7647/abd4ef>.
  26. Menon, R., Gil, D., Barbastathis, G., Smith, H. I. (2005). Photon-sieve lithography. *J. Opt. Soc. Am. A*, 22(2), 342–345. <https://doi.org/10.1364/josaa.22.000342>.
  27. Janeiro, R., Flores, R., Dahal, P., & Viegas, J. (2016). Fabrication of a phase photon sieve on an optical fiber tip by focused ion beam nanomachining for improved fiber to silicon photonics waveguide light coupling. *Opt. Express*, 24(11), 11611–11625. <https://doi.org/10.1364/oe.24.011611>.
  28. Vijayakumar, A., Kashter, Y., Kelner, R., Rosen, J. (2016). Coded aperture correlation holography—a new type of incoherent digital holograms. *Opt. Express* 24(11), 12430-12441. <https://doi.org/10.1364/OE.24.012430>.
  29. Vijayakumar, A., Rosen, J. (2017). Interferenceless coded aperture correlation holography—a new technique for recording incoherent digital holograms without two-wave interference. *Opt. Express* 25(12), 13883-13896. <https://doi.org/10.1364/OE.25.013883>.
  30. Rai, M. R., Vijayakumar, A., Rosen, J. (2018). Non-linear adaptive three-dimensional imaging with interferenceless coded aperture correlation holography (I-COACH). *Opt. Express*, 26(14), 18143–18154. <https://doi.org/10.1364/oe.26.018143>.
  31. Wan, Y., Liu, C., Ma, T., Qin, Y., lv, S. (2021). Incoherent coded aperture correlation holographic imaging with fast adaptive and noise-suppressed reconstruction. *Opt. Express*, 29(6), 8064–8075. <https://doi.org/10.1364/oe.418918>.
  32. Vijayakumar, A., Katkus, T., Lundgaard, S., P. Linklater, D., P. Ivanova, E., Hock Ng, S., Juodkazis, S. (2020). Fresnel incoherent correlation holography with single camera shot. *Opto-Electron. Adv.*, 3(8), 200004–200004. <https://doi.org/10.29026/oea.2020>.
  33. Buividas, R., Mikutis, M., Juodkazis, S. (2014). Surface and bulk structuring of materials by ripples with long and short laser pulses: Recent advances. *Prog. Quantum Electron*, 38(3), 119–156. <https://doi.org/10.1016/j.pquantelec.2014.03.002>.
  34. Gamaly, E. G., Rode, A. V. (2018). Ultrafast re-structuring of the electronic landscape of transparent dielectrics: new material states (Die-Met). *Appl. Phys. A*, 124(3), 1–11. <https://doi.org/10.1007/s00339-018-1693-3>.
  35. Juodkazis, S., Nishi, Y., Misawa, H. (2008). Femtosecond laser-assisted formation of channels in sapphire using KOH solution. *Phys. Status Solidi-R*, 2(6), 275–277. <https://doi.org/10.1002/pssr.200802203>.
  36. Anand, V., Ng, S. H., Maksimovic, J., Linklater, D., Katkus, T., Ivanova, E. P., Juodkazis, S. (2020). Single shot multispectral multidimensional imaging using chaotic waves. *Sci. Rep.*, 10(1), 13902. <https://doi.org/10.1038/s41598-020-70849-7>.
  37. Vanagas, E., Kawai, J., Tuzilin, D., Kudryashov, I., Mizuyama, A., Nakamura, K. G., Kondo, K., Koshihara, S., Takesada, M., Matsuda, K., Juodkazis, S., Jarutis, V., Matsuo, S., & Misawa, H. (2004). Glass cutting by femtosecond pulsed irradiation,” *J. Microlith. Microfab. Microsyst.* 3(2), 358–363.
  38. Maksimovic, J., Ng, S.-H., Katkus, T., An Le, N. H., Chon, J. W. M., Cowie, B. C. C., Yang, T., Bellouard, Y., Juodkazis, S. (2020). Ablation in Externally Applied Electric and Magnetic Fields. *Nanomaterials*, 10(2), 182. <https://doi.org/10.3390/nano10020182>.
  39. Maksimovic, J., Ng, S. H., Katkus, T., Cowie, B. C., Juodkazis, S. (2019). External Field-Controlled Ablation: Magnetic Field. *Nanomaterials*, 9(12), 1662. <https://doi.org/10.3390/nano9121662>.
  40. Hua, J.-G., Ren, H., Jia, A., Tian, Z.-N., Wang, L., Juodkazis, S., Chen, Q.-D., Sun, H.-B. (2020). Convex silica microlens arrays via femtosecond laser writing. *Opt. Lett.*, 45(3), 636–639. <https://doi.org/10.1364/ol.378606>.
  41. Hua, J.-G., Tian, Z.-N., Xu, S.-J., Lundgaard, S., Juodkazis, S. (2019). Fast fabrication of optical vortex generators by femtosecond laser ablation. *Appl. Surf. Sci.*, 475, 660–665. <https://doi.org/10.1016/j.apsusc.2018.12.249>.
  42. Bundy, K., et. al. (2019). FOBOS: A Next-Generation Spectroscopic Facility at the WM Keck Observatory. *arXiv preprint arXiv:1907.07195*. 2019 Jul 16.
  43. Caramazza, P., Moran, O., Murray-Smith, R., Faccio, D. (2019). Transmission of natural scene images through a multimode fibre. *Nat. Commun.* 10, 2029. <https://doi.org/10.1038/s41467-019-10057-8>.